

Electronic Supplementary Information

An Autonomously Ultrafast Self-Healing, Highly Colorless, Tear-Resistant and Compliant Elastomer Tailored for Transparent Electromagnetic Interference Shielding Films Integrated in Flexible and Optical Electronics

FuYao Sun,^{a,b} JianHua Xu,^{*a,b} Tong Liu,^b FeiFei Li,^c Yin Poo^{*c}, YaNa Zhang^b, RanHua Xiong^a, ChaoBo Huang^a and JiaJun Fu,^{*b}

^a**Joint Laboratory of Advanced Biomedical Materials (NFU-UGent), College of Chemical Engineering, Nanjing Forestry University, 210037, China.**

^b**School of Chemical Engineering, Nanjing University of Science and Technology, 210094, China.**

^c**School of Electronic Science and Engineering, Nanjing University, 210023, China.**

***Corresponding author. E-mail: jianhuaxu@njfu.edu.cn; fujiajun668@gmail.com; ypoo@nju.edu.cn.**

General characterization

^1H NMR spectra were recorded on Bruker AVANCE III 500 MHz spectrometer at room temperature with tetramethylsilane (TMS) as an internal reference. ATR-FTIR spectra were recorded on a Bruker Tensor II spectrometer that equipped with a Specac Golden Gate ATR heating/cooling cell in the range of 4000-1000 cm^{-1} . Thermo Scientific E220 UV-vis spectrophotometer was applied to determine transparency. SAXS measurements were conducted on Bruker AXS NanoSTAR instrument equipped with a microfocus X-ray source, operating at $\lambda=0.1541\text{nm}$. TGA was carried out on a TA TGA-550 instrument with a heating rate of $20\text{ }^\circ\text{C min}^{-1}$ in nitrogen atmosphere from 50 to 800 $^\circ\text{C}$. DSC measurement was performed on a TA DSC-25 differential scanning calorimeter at the heating rate of $20\text{ }^\circ\text{C min}^{-1}$. GPC was carried out in THF on PolyPore columns (Agilent) connected in series with a DAWN multiangle laser light scattering (MALLS) detector and an Optilab TrEX differential refractometer (both from Wyatt Technology). FESEM measurements were performed with a JEOL 7800F field emission electron microscope under an acceleration voltage of 2 kV. Optical microscopy images for illustrating the self-healing of scratches were recorded using a Jiangnan MV3000 optical microscope. The sheet resistances were measured by RTS-9 4-point probes resistivity measurement system (4 PROBES TECH). Strain-dependent resistance was measured by Keithley 2450 source measure unit connecting with the Ag NWs/PDMS-MPI-HDI films by conductive tapes. EMI shielding properties were measured by N5230A network analyzer utilizing the wavelength at the X-band (8.2–12.4 GHz) and the C-band (4.25–5.99 GHz), Ag NWs/PDMS-MPI-HDI films were cut into slightly larger dimensions compared to the waveguide window. As for strain-dependent EMI shielding properties, one of two waveguides was fixed in the middle of the tensile tester with their surface kept even. Both ends of the Ag NWs/PDMS-MPI-HDI films were fixed on the tensile tester and their EMI shielding properties were measured at different strain.

Mechanical characterization.

Tensile tests were conducted on a Shimadzu AGS-X tester at 25 $^\circ\text{C}$ with a strain rate of 100 mm min^{-1} . Three samples with a tensile size of 10 mm gauge length \times 10 mm width \times 0.8-1.2 mm thickness were tested for each polymer composition, and their average value was given. The speed-dependent tensile tests were performed with variable strain rate of 100 mm min^{-1} , 200 mm min^{-1} , 400 mm min^{-1} and 800 mm min^{-1} . For the cyclic tensile test, both loading and unloading process were performed at a strain rate of 100 mm min^{-1} at 25 $^\circ\text{C}$.

DMA was measured using a TA Q800 instrument in the film tension geometry. Dimensions of the samples for DMA measurements were determined by a standard Vernier calliper. The length of the sample between the tensile clamps was determined by the DMA instruments itself. The temperature sweep experiments were conducted under tension condition with a frequency of 1 Hz. The scanning temperature ranged from -100-150 $^\circ\text{C}$ at a heating rate of $5\text{ }^\circ\text{C min}^{-1}$. For stress relaxation experiment, three samples were quickly stretched to 100% strain and then set at this strain for relaxation for 10 min. Subsequently, the applied stress on those samples were gradually relaxed in different degree.

Bulk rheological measurements were performed on TA DHR-1 Rheometer (20 mm parallel steel plate). Frequency sweeps were performed at a strain amplitude of 0.1% by varying the frequency between 0.1 rad s^{-1} to 100 rad s^{-1} in a temperature range of 25-135 $^\circ\text{C}$.

Self-healing testing

For self-healing tests, a tensile spline was cut into two completely separate pieces with a razor blade. Then, the cut faces were gently contacted together without any press and left under ambient conditions for various healing times. Subsequently, the self-healed samples were subjected to a tensile-stress test at 25 °C with a tensile rate of 100 mm min⁻¹. The healing efficiency is calculated from the ratio of the integral areas under stress-strain curves of healed films to that of the virgin film.^[1] The measurements were performed using more than three splines for each healing time to achieve the average value.

For self-healing tests of conductivity, both ends of rectangular Ag NWs/PDMS-HDI films (30 mm length, 8 mm width and 0.5 mm thickness) were attached to conductive tapes on the coaxial tensile tester, leaving a length of 10 mm in the middle. Then, those films were cut in half by razor blade and connected again for self-healing, the change in resistance was detected by the Keithley 2450 source measure unit.

Towards self-healing tests of EMI properties, rectangular Ag NWs/PDMS-MPI-HDI films with 75 mm length, 25 mm width and 0.5 mm thickness were applied a notch of 5 mm. The notched films were fixed at a tensile tester that equipped with a N5230A network analyzer waveguide, the EMI shielding effectiveness of the notched films were tested under different strain (0%, 50%). Subsequently, the stretched films were released to 0% strain, and two notched surfaces were self-connected to achieve self-healing at 25 °C for 20 minutes. Finally, the healed film was stretched to 50% strain again, and their EMI shielding effectiveness was recorded accordingly.

1. Supplementary Figures

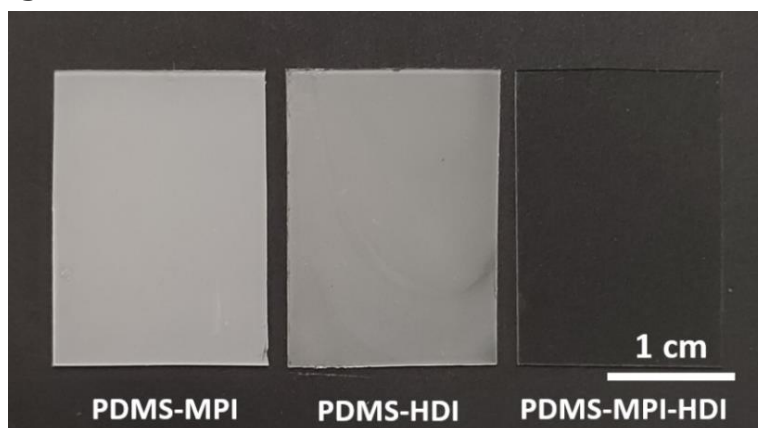


Fig. S1 Digital photographs of PDMS-MPI, PDMS-HDI and PDMS-MPI-HDI films. These three films were prepared by pouring hot and concentrated solution onto the clean glass sheet and drying at room temperature. As shown, the prepared PDMS-MPI-HDI film is colorless and transparent, indicating its amorphous structure. For comparison, the control PDMS-MPI and PDMS-HDI films are opaque, suggesting the crystalline behavior.

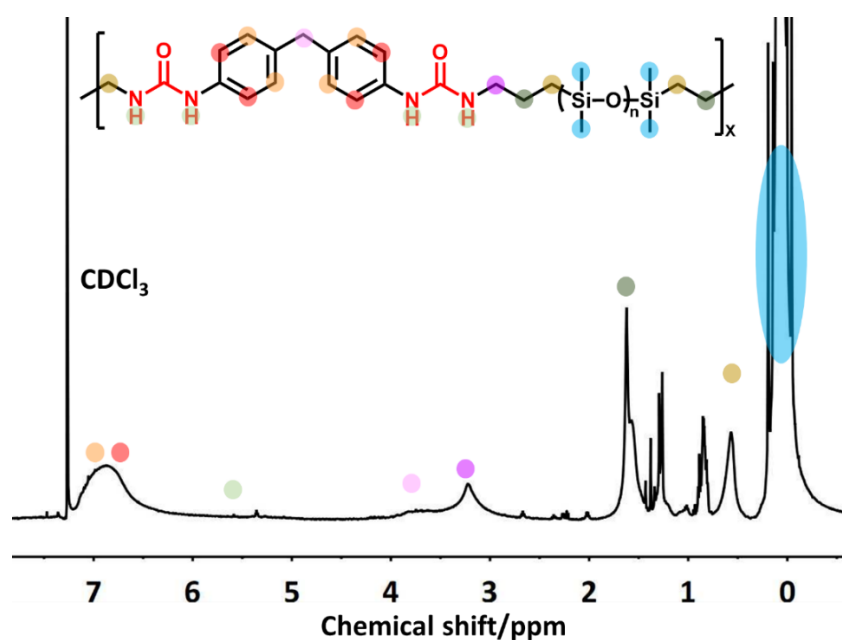


Fig. S2 ¹H NMR spectra of PDMS-MPI (500 MHz, CDCl₃, 298 K).

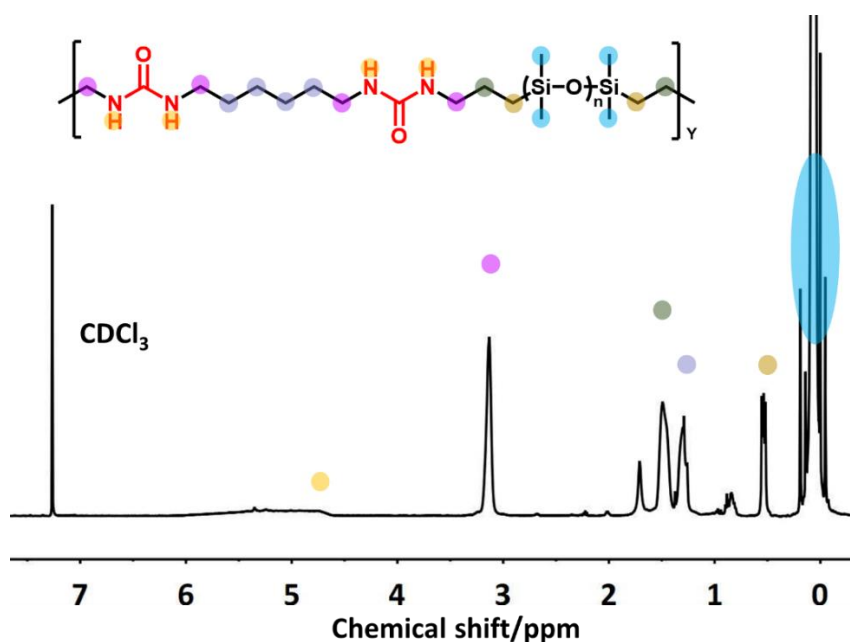


Fig. S3 ^1H NMR spectra of PDMS-HDI (500 MHz, CDCl_3 , 298 K).

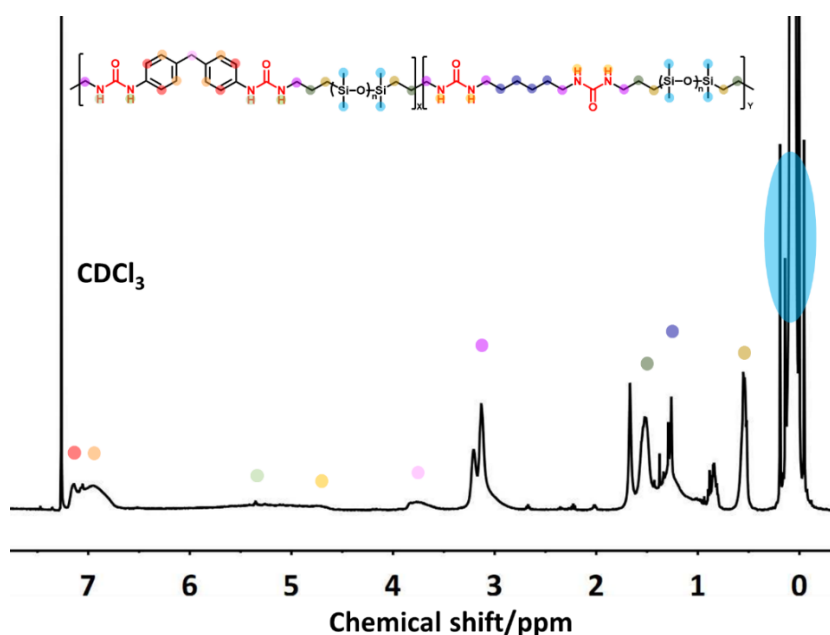


Fig. S4 ^1H NMR spectra of PDMS-MPI-HDI (500 MHz, CDCl_3 , 298 K).

^1H NMR demonstrates the successful synthesis of PDMS-based polyurea, including PDMS-MPI, PDMS-HDI and PDMS-MDI-HDI (Fig. S2-S4). Specifically, the NH proton signals of the urea motifs emerge in the range of 4.5-6.0 ppm in CDCl_3 .^[2] Besides, the methylene groups adjacent to PDMS chains are identified at 0.54 ppm, and the methylene groups adjacent to urea motifs are centered at 3.07 ppm. In the case of introducing MPU motifs during synthesis, the resonance of aromatic protons appeared between 6.85 and 7.10 ppm. In contrast, for introducing HDU motifs during synthesis, the resonance of aliphatic protons emerged between 1.02 and 1.50 ppm.

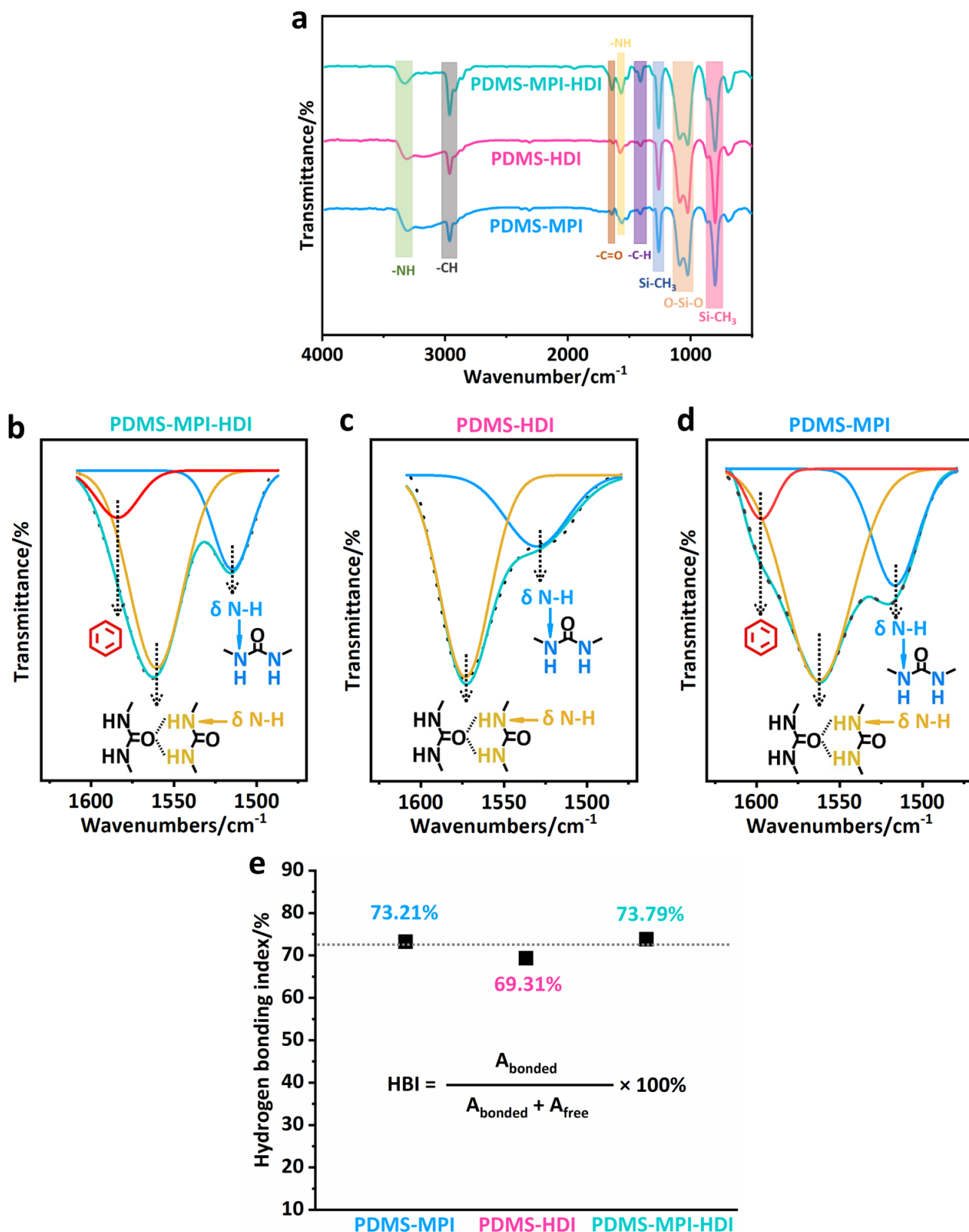


Fig. S5 (a) FT-IR spectra of the prepared PDMS-MPI-HDI, PDMS-MPI and PDMS-HDI. Deconvolution of FT-IR spectra of (b) PDMS-MPI-HDI, (c) PDMS-HDI and (d) PDMS-MPI. (e) Hydrogen bonding index of PDMS-MPI-HDI, PDMS-MPI and PDMS-HDI. As shown Figure S5a, all three FT-IR spectra show the absence of stretching vibration of free isocyanate moieties (ν_{NCO}) that is

usually centered around 2265 cm^{-1} ,^[3] suggesting the complete reaction between $-\text{NCO}$ and $-\text{NH}_2$ groups. Besides, the successful synthesis of PDMS-based polyureas was demonstrated by the appearance of characteristic peaks of the generated urea moieties between $1700\text{--}1500\text{ cm}^{-1}$ related to urea amide I and amide II region, and between $3400\text{--}3200\text{ cm}^{-1}$ typical for the stretching vibration of $\nu_{\text{N-H}}$.^[2] For all investigated polymers, their FT-IR spectra also contain characteristic peaks of PDMS soft chains ranging from $1400\text{--}800\text{ cm}^{-1}$,^[4] further proving the successful synthesis of PDMS-MPI, PDMS-HDI and PDMS-MPI-HDI films. In the following, we further employ FT-IR to investigate the different hydrogen bonds in the prepared PDMS-based polyureas, which are closely related to the microphase separation structure. Specifically, the bond characteristics for in-plane bending vibration of $\delta_{\text{N-H}}$ from $1620\text{--}1480\text{ cm}^{-1}$ caught our attention. To determine the contents of free and bonded N-H motifs, their vibration regions were divided accordingly by Peakfit 4.0. Figure S5(b-d) show the typical curve-fitting procedures, and the characteristic peaks for bonded and free N-H motifs are clearly identified. We employ hydrogen bonding index (HBI) to indicate the microphase separation,^[5] which was defined by formula inserted in Fig. S5e, where A_{bonded} is the absorption peak area of bonded N-H, and the A_{free} is assigned to the free N-H motifs. As shown in Fig. S5e, the HBI of PDMS-MPI-HDI and its "parent" polymers are almost similar, with the values waving around 70%, indicating a high degree of hydrogen bonding between urea-urea groups within hard domains. These results imply almost the same H-bonding cross-linkings for PDMS-MPI, PDMS-HDI and PDMS-MPI-HDI.

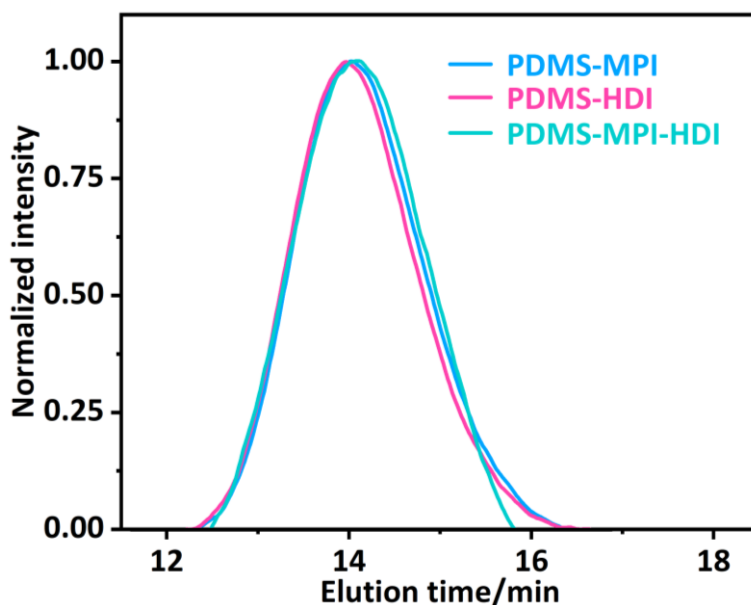


Fig. S6 GPC curves of PDMS-MPI, PDMS-HDI and PDMS-MPI-HDI,

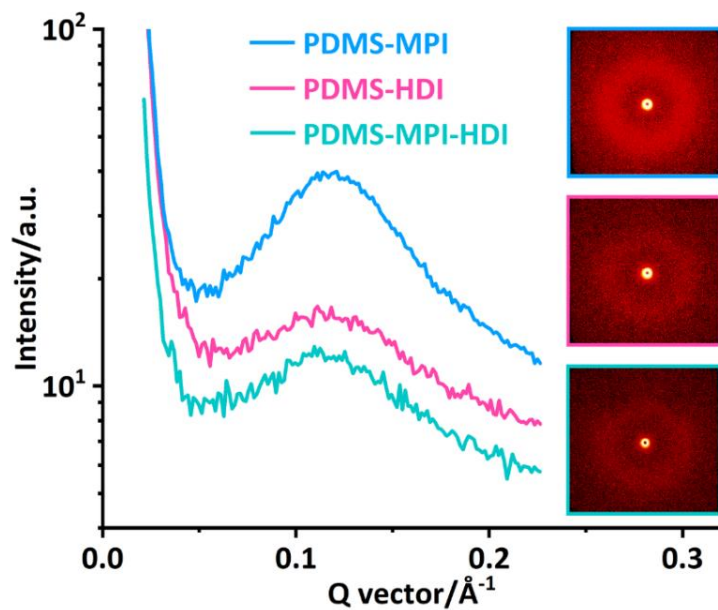


Fig. S7 SAXS spectra of PDMS-MPI, PDMS-HDI and PDMS-MPI-HDI

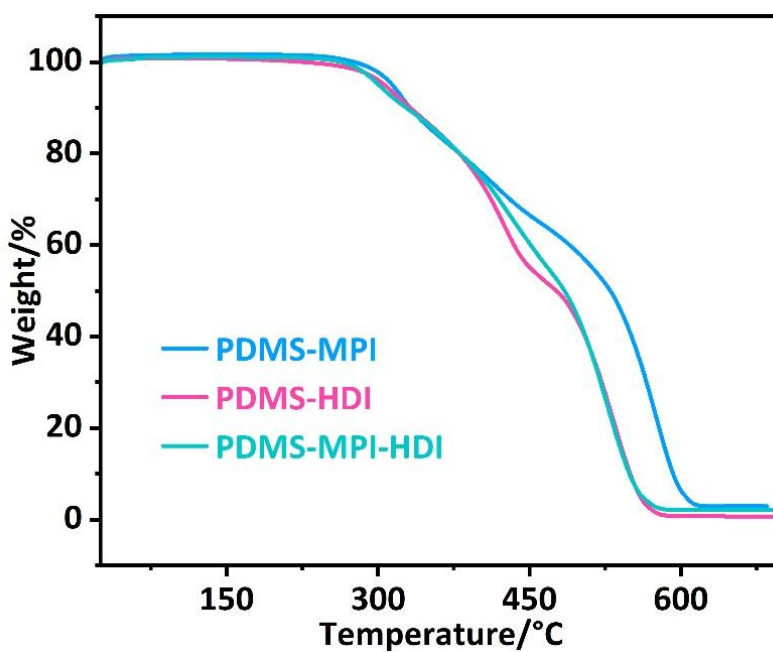


Fig. S8 TG curves of PDMS-MPI, PDMS-HDI and PDMS-MPI-HDI. As shown, all three films start to lose weight at about 250 °C, suggesting the excellent thermal stability.

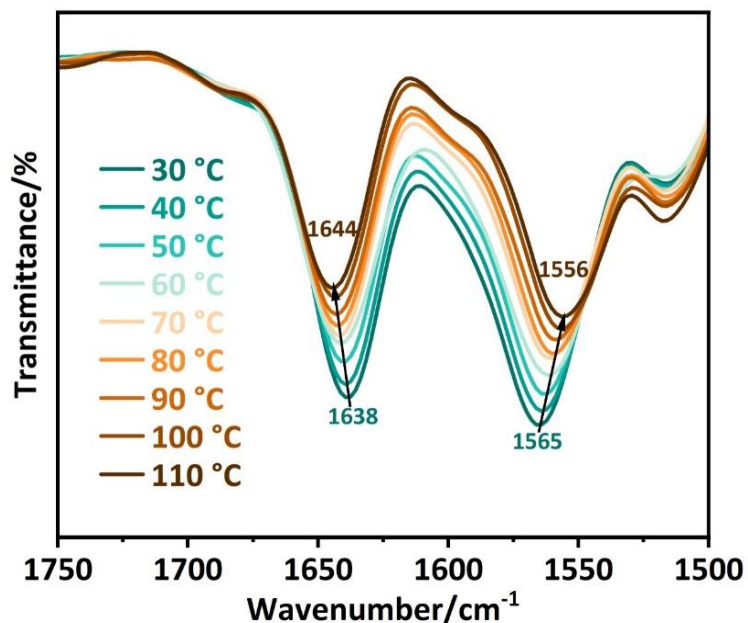


Fig. S9 Temperature-dependent FT-IR spectra of PDMS-MPI-HDI. As shown, when the temperature increases from 30 to 110°C, the stretching vibration peak of C=O at 1638 cm^{-1} gradually shifted to 1644 cm^{-1} , whereas the flexural vibration peak of N-H shifted from 1565 cm^{-1} to 1556 cm^{-1} , confirming the formation of hydrogen bonds between different urea groups within hard domains.^[6]

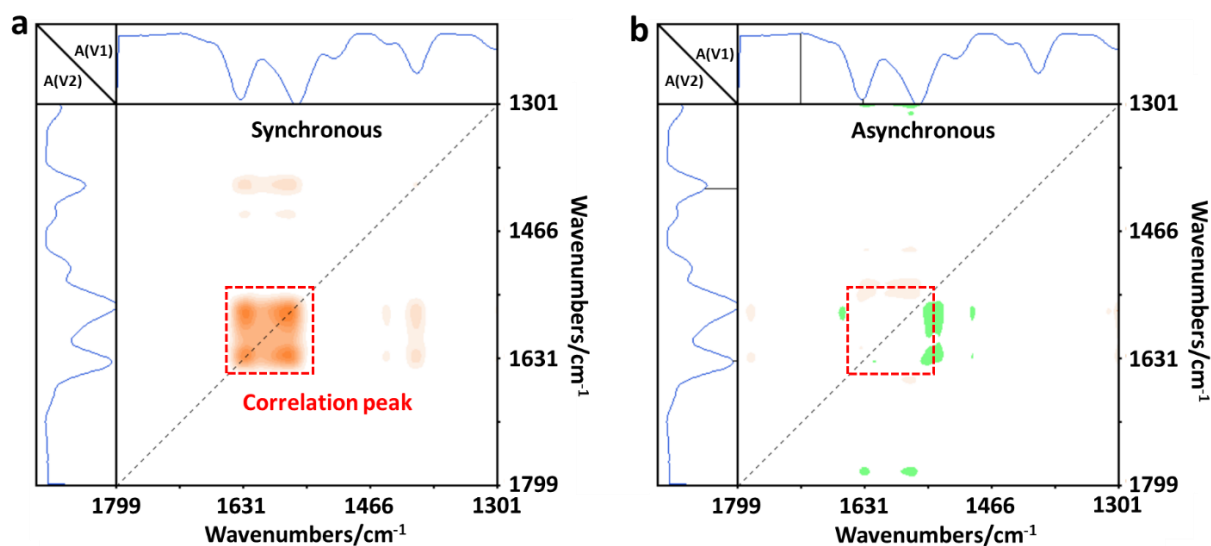


Fig. S10 (a) Synchronous and (b) asynchronous 2D correlation FT-IR spectra of PDMS-MPI-HDI calculated from Fig. S9

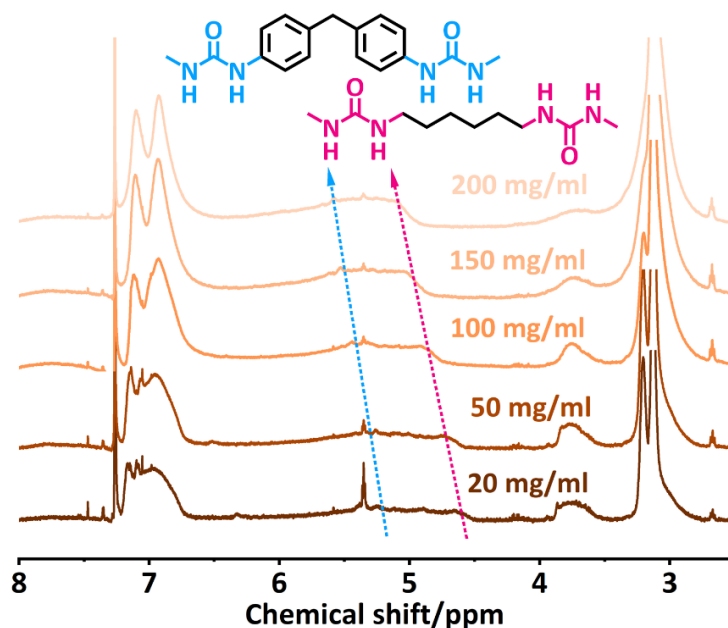


Fig. S11 Concentration-dependent ^1H NMR spectra of PDMS-MPI-HDI

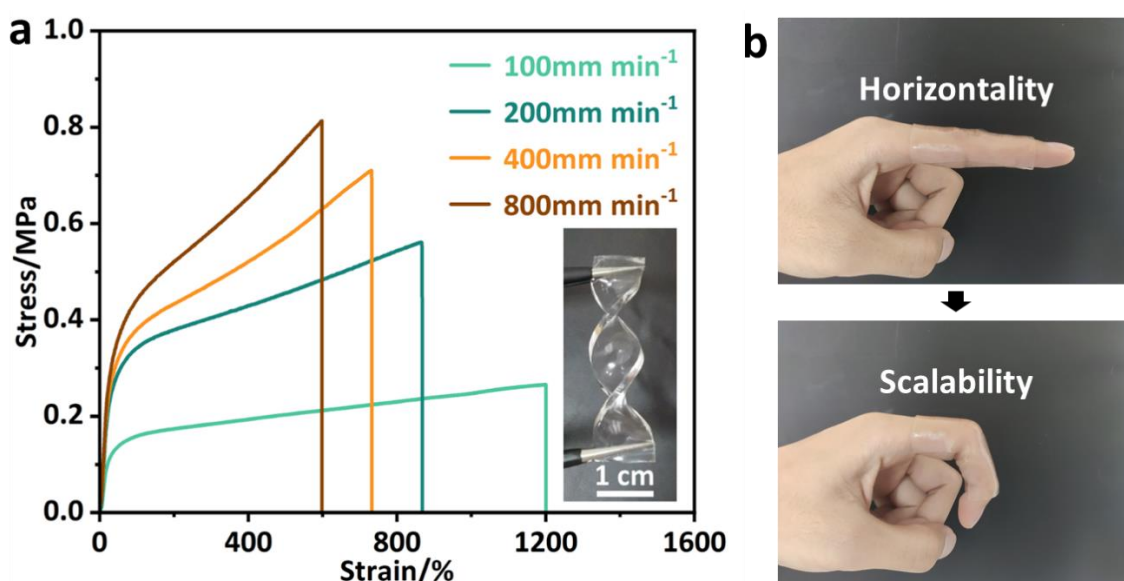


Fig. S12 (a) Tensile stress–strain curves of PDMS-MPI-HDI under different deformation rates; inset photograph showing the compliance of PDMS-MPI-HDI. **(b)** A piece of stretchable PDMS-MPI-HDI elastomer can conform to a human finger under large strains. As the deformation rate increased from 100 mm min^{-1} to 800 mm min^{-1} , the Young's modulus of PDMS-MPI-HDI gradually increased from 0.75 MPa to 1.57 MPa , while their elongations at break decreased from 1200% to 598% accordingly (Fig.S12a). These phenomena were attributed to the fact that the multiple hierarchical H-bonds within dynamic hard domains did not have sufficient time to recombine after rupture at time scale.^[7] Satisfactorily, the Young's of PDMS-MPI-HDI is small enough (1.57 MPa) even under a high tensile rate of 800 mm min^{-1} , demonstrating its superior compliance, which is further verified by the inset photograph in Fig. S12a and Fig. S12b.

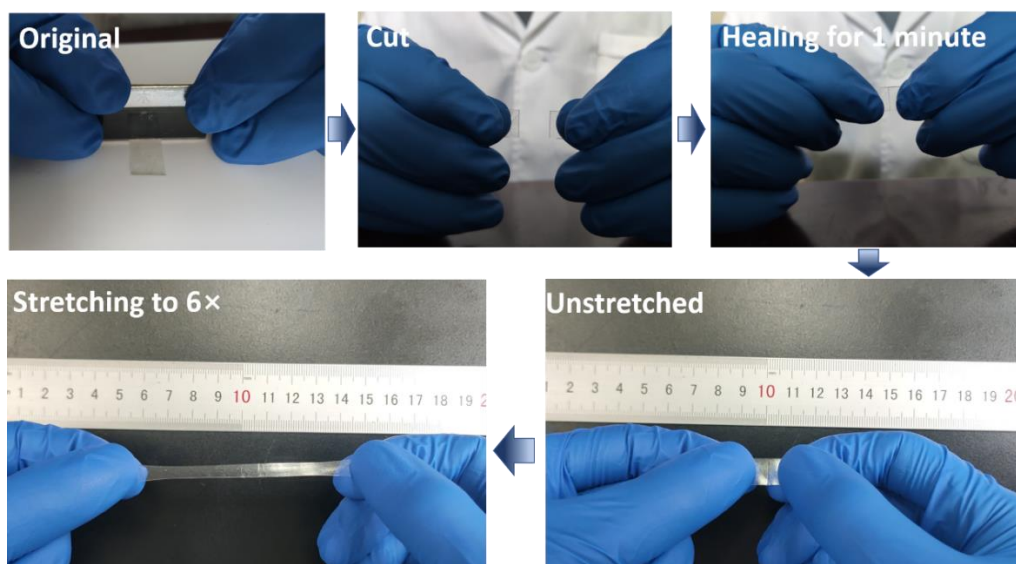


Fig. S13 Photographs showing the ultrafast self-healing behavior of the PDMS-MPI-HDI film.

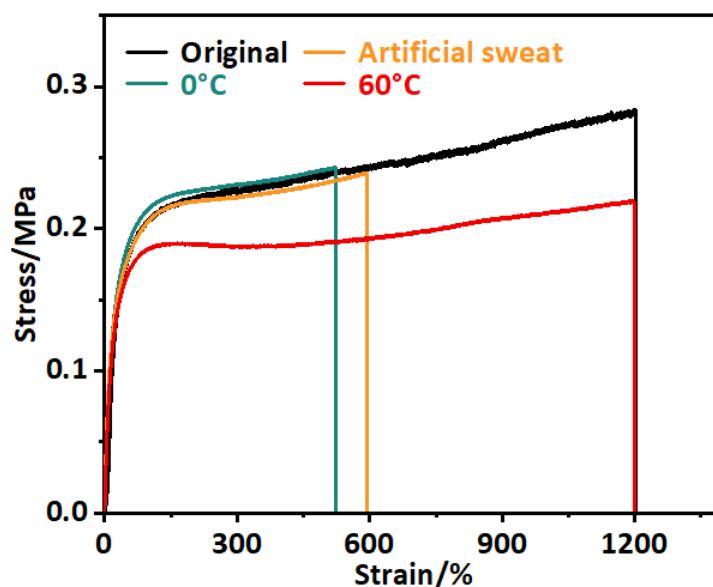


Fig. S14 Tensile curves of the original and self-healed PDMS-MPI-HDI for 1 minute at different harsh environments. As shown, compared with the 1 min self-healing efficiency at 25 °C, the corresponding self-healing efficiencies at 60 °C and 0 °C are 81.27% and 39.94%, respectively. The improved self-healing efficiency at high temperature is mainly due to the synergistic effect of the enhanced chain mobility as well as the fast dynamics of the hydrogen bonds within hard domains. Besides, healing under artificial sweat for 1 min exhibited a self-healing efficiency of 44.32%, which is almost the same value as the 1 min self-healing efficiency at 25 °C, suggesting that water molecules have little effect on the self-healing ability of PDMS-MPI-HDI due to excellent hydrophobic performance of PDMS polymer.

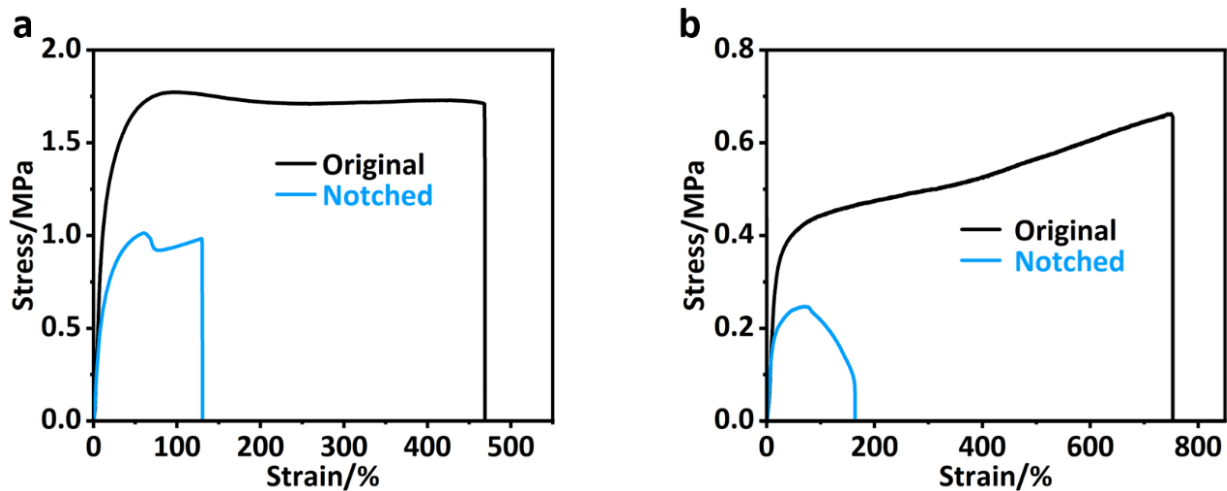


Fig. S15 Tensile curves of the original and notched (a)PDMS-MPI (b) PDMS-HDI films

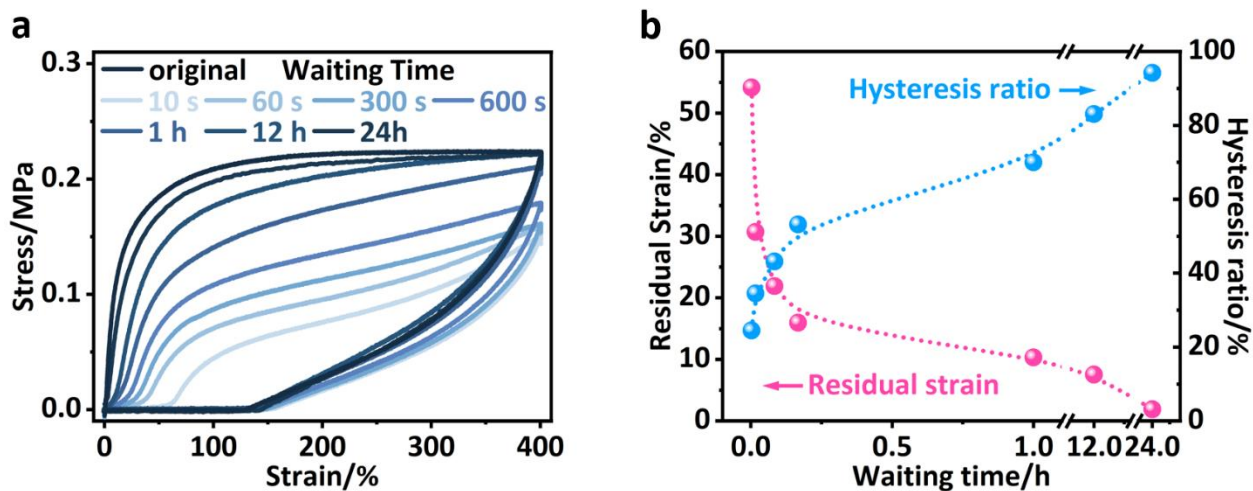


Fig. S16. Cyclic tensile properties of PDMS–MPI–HDI. (a) Recovery curves for different waiting times performed by cyclic tensile test with the maximum strain of 400%. (b) Waiting time dependence of the corresponding hysteresis ratio and residual strain with the maximum of 400%.

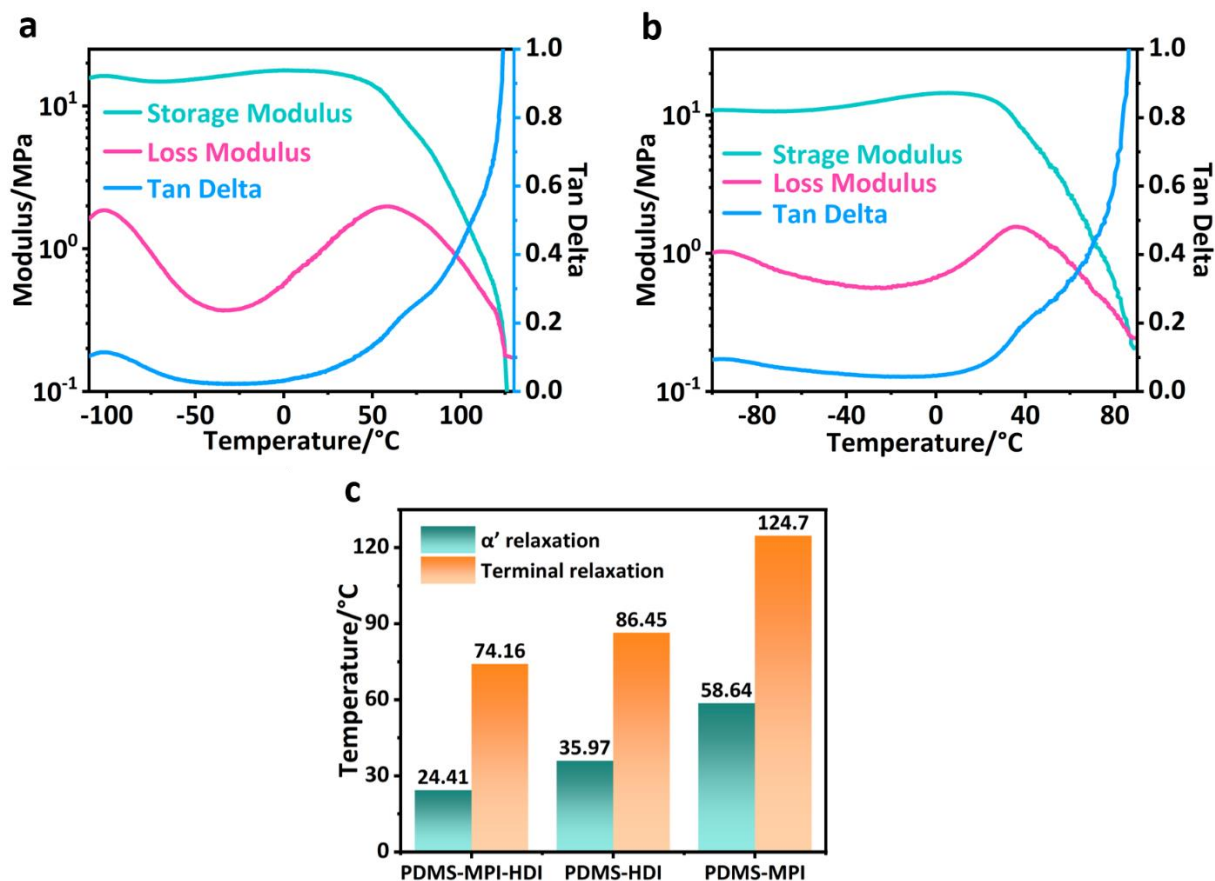


Fig. S17. Storage modulus, loss modulus and loss factor versus temperature for (a) PDMS-MPI and (b) PDMS-HDI at a heating rate of 5 °C min⁻¹. (c) Comparison of temperature of α' relaxation and terminal relaxation of PDMS-MPI-HDI, PDMS-HDI and PDMS-MPI.

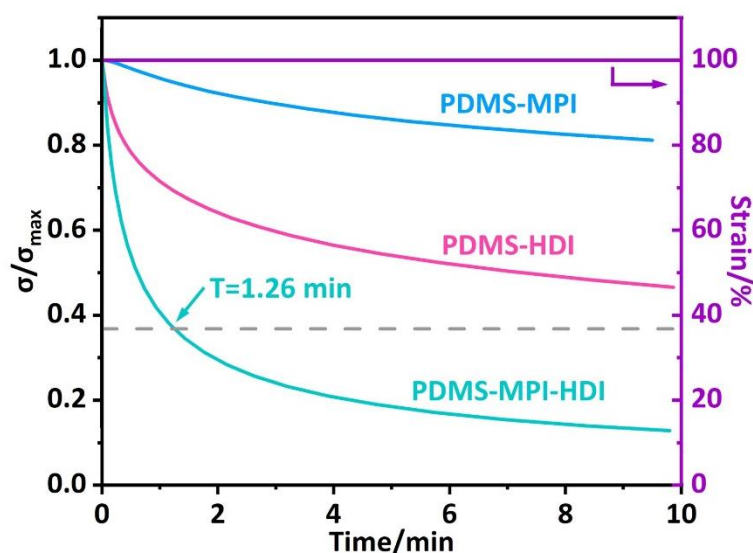


Fig. S18 Stress relaxation curves of PDMS-MPI, PDMS-HDI and PDMS-MPI-HDI to 100% strain at 25 °C. As shown, the stress relaxation rate of PDMS-MPI-HDI is much faster its “parent” polymers (PDMS-MPI, PDMS-HDI), providing strong evidence of its fast chain dynamics at room temperature.

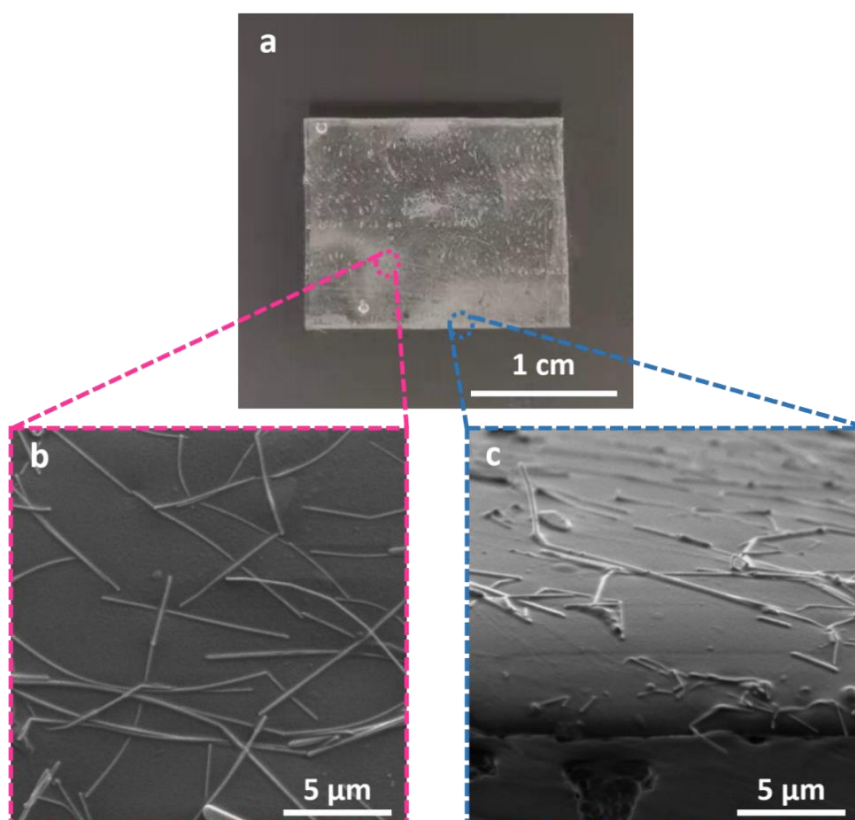


Fig. S19 (a) Digital photograph and (b, c) the corresponding SEM images of Ag NWs coating on the sylgard 184 substrate. As shown in Fig. S19a, the distribution of Ag NWs coated on sylgard 184 substrate is extremely uneven, attributed to the weak interaction between Ag NWs and sylgard 184 substrate. Moreover, SEM was employed to observe the microstructure of the selected areas with more Ag NWs and the corresponding images are showed in Fig. S19b and S19c. As depicted, Ag NWs are just simply coated on the surface of sylgard 184, rather than embedded, which is totally different from the microstructure of Ag NWs/PDMS-MPI-HDI in Figure 1f.

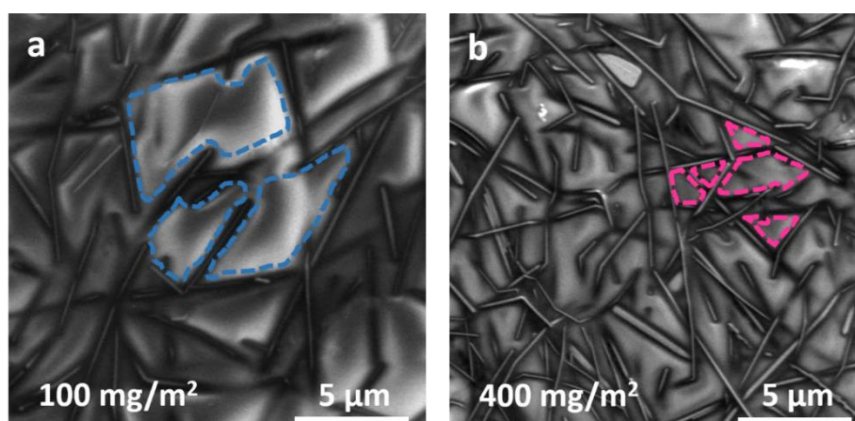


Fig. S20 SEM images of Ag NWs percolation network embedded into PDMS-MPI-HDI with different area density; (a) 100 mg/m², (b) 400 mg/m². As shown, the voids in Ag NWs percolation network gradually decreased with the increase of Ag NWs area densities, leading to the reduction of transparency.

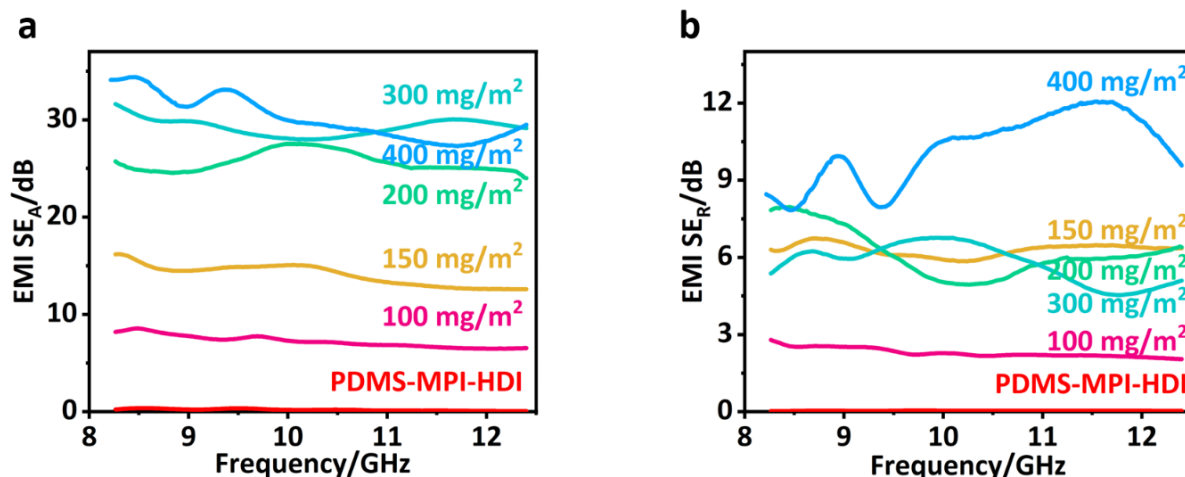


Fig. S21 (a) Absorption and (b) reflection EMI shielding effectiveness of Ag NWs/PDMS-MPI-HDI with different Ag NWs area densities. As shown, the SE_A value in the whole X-band (8.2-12.4 Hz) increased gradually with the increase of Ag NWs area densities, while the SE_R just changed a little, demonstrating the absorption-dominated shielding mechanism of Ag NWs/PDMS-MPI-HDI.

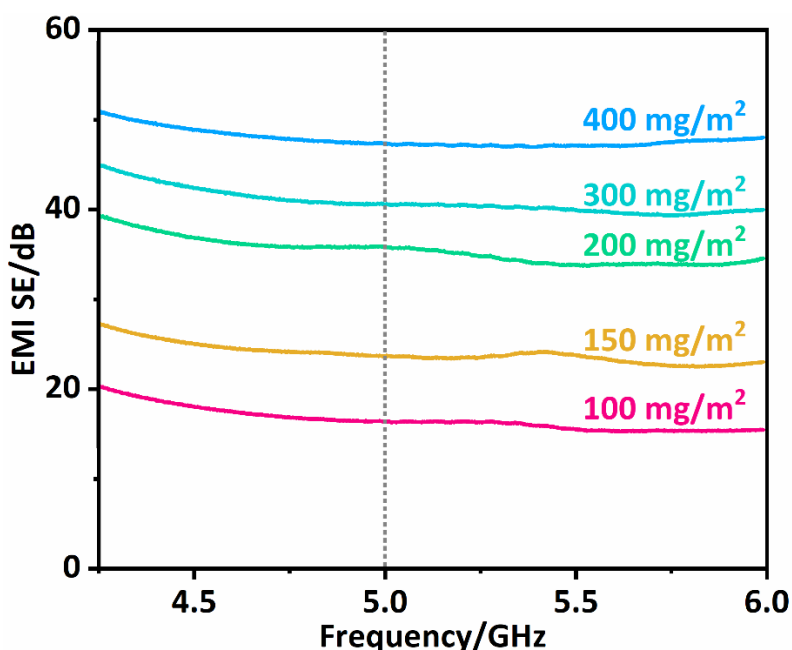


Fig. S22 EMI shielding effectiveness as a function of frequency for different Ag NWs/PDMS-MPI-HDI films at 4.25-5.99 GHz. As shown, the overall EMI SE of different Ag NWs/PDMS-MPI-HDI films at 4.25-5.99 GHz gradually enhance with the increase of Ag NWs area densities, which is consistent with the variations at X-band shown in Fig. 4d. For Ag NWs-100/PDMS-MPI-HDI, its average EMI SE at 5 GHz is ~16.42 dB, corresponding a relatively low shielding efficiency of 97.72%. However, as the Ag NWs area densities increase to >150 mg m⁻², the overall EMI SEs of all the Ag NWs/PDMS-MPI-HDI are always >20 dB (shielding efficiency >99%), demonstrating their potentials used in IOT devices.

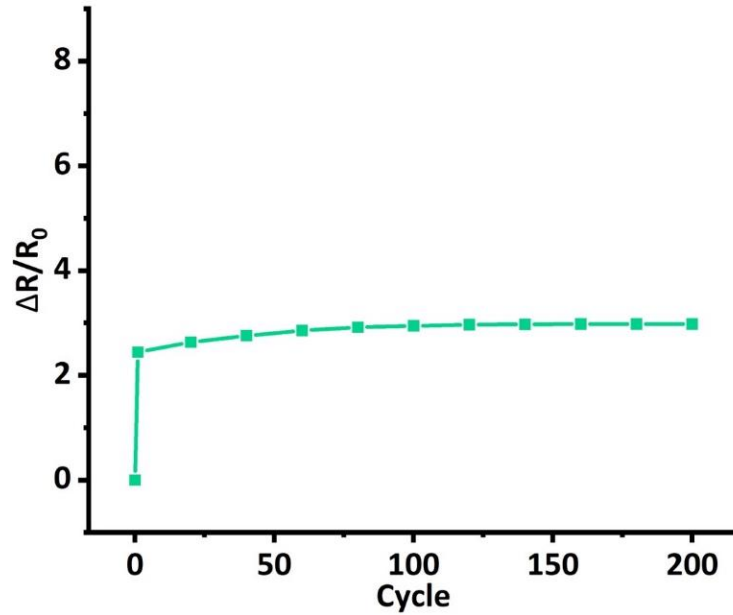


Fig. S23 Sheet resistance changes during cyclic stretching. As shown, the sheet resistance of Ag NWs-200/PDMS-MPI-HDI slightly increases with the increase of stretching-retracting cycles, and eventually turns into a constant value, demonstrating its long-term resistance stability.

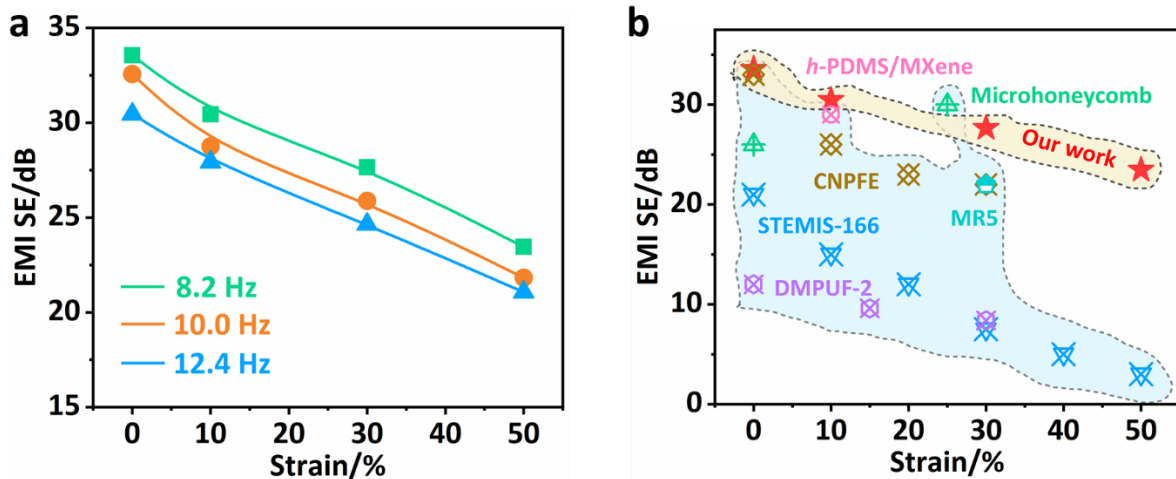


Fig. S24 (a) EMI SE plotted under various strains for Ag NWs-200/PDMS-MPI-HDI. (b) Comparison of tensile strain and EMI SE at 8.2 Hz. Fig. S24a exhibits the EMI SE of Ag NWs-200/PDMS-MPI-HDI under various strain at X band (8.2, 10.0, 12.4 Hz). As depicted, the EMI SE gradually decreases with the increase of tensile strain, but it is always >20 dB to 50% strain. Then, we compare the stretching EMI SE of Ag NWs-200/PDMS-MPI-HDI with other stretchable EMI shielding materials, which is presented in Figure S24b. By contrast, our Ag NWs-200/PDMS-MPI-HDI possess good stretching EMI SE, i.e., it demonstrates high EMI SE with large strain, which is comparable to previously reported works.^[8-13]

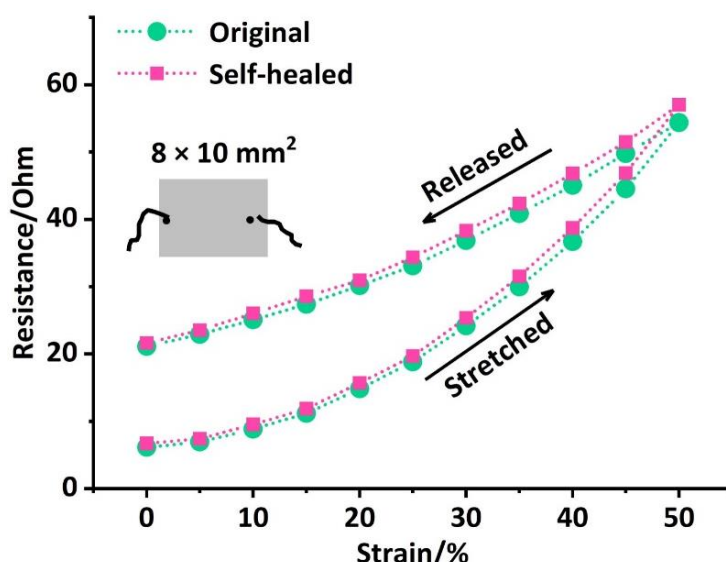


Fig. S25 Strain-dependent resistance variations of the original and self-healed Ag NWs-200/PDMS-MPI-HDI up to 50% strain. As shown, the resistance variations of the self-healed sample during stretching-retracting cycle are basically the same as the pristine one, confirming the excellent self-healing ability of the tensile conductivity of Ag NWs-200/PDMS-MPI-HDI.

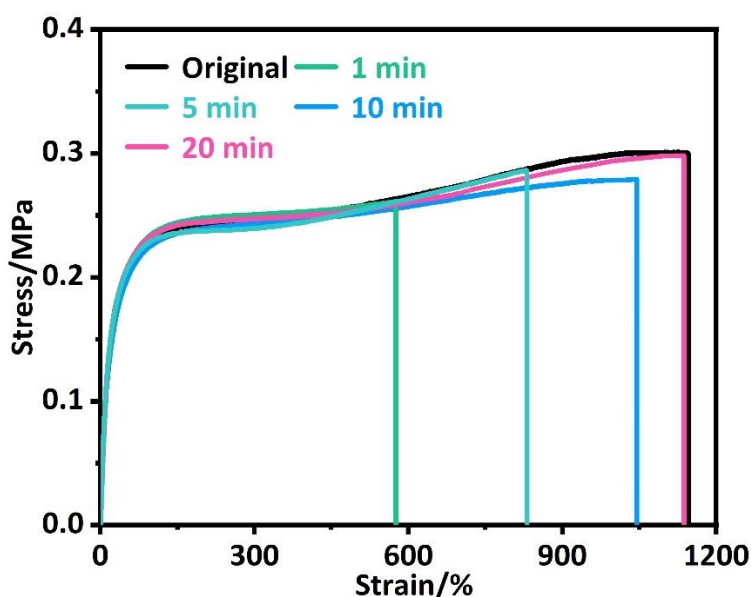


Fig. S26 Typical stress-strain curves of the original and healed Ag NWs-200/PDMS-MPI-HDI for different healing time at room temperature. As shown, the tensile curve of the pristine Ag NWs-200/PDMS-MPI-HDI is almost the same as the original PDMS-MPI-HDI sample, suggesting the negligible influence of the embedded thin Ag NWs coating on the overall mechanical properties. Meanwhile, the healing efficiencies of Ag NWs-200/PDMS-MPI-HDI increase with the prolongation of healing times. As expected, Ag NWs-200/PDMS-MPI-HDI possesses a high self-healing efficiency of 87.10% after healing for 10 min, which is slightly smaller than that of PDMS-MPI-HDI due to the inhibition of surface-embedded Ag NWs. However, when the healing time prolongs to 20 min, the damaged Ag NWs-200/PDMS-MPI-HDI sample can fully restores its mechanical properties, with a self-healing efficiency waving around 100%.

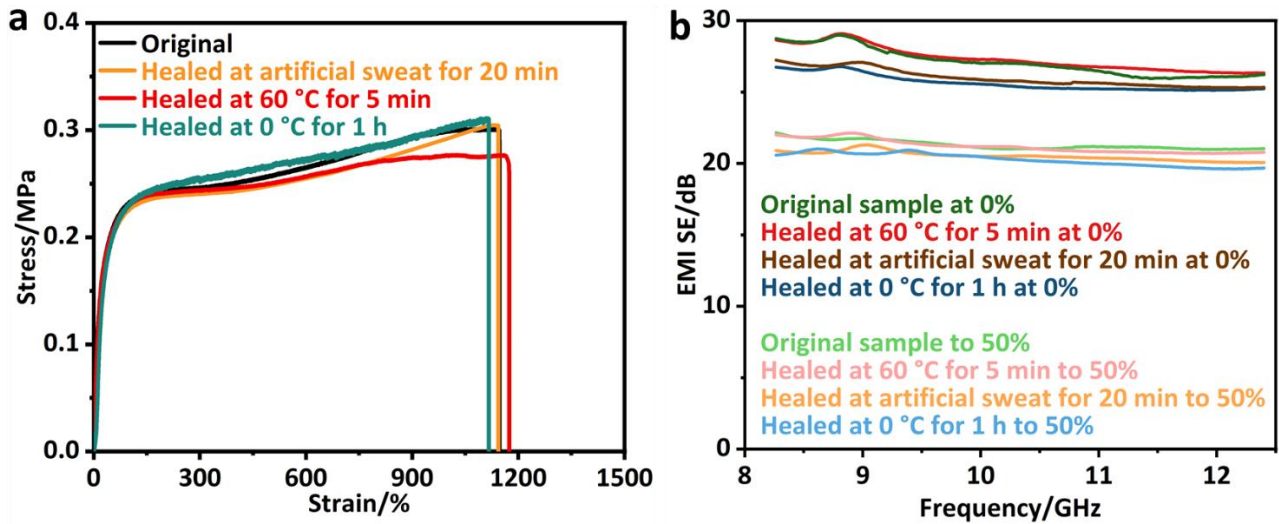


Fig. S27 (a) Tensile curves of the original and self-healed PDMS-MPI-HDI at different harsh environments; (b) EMI SE of the original and self-healed Ag NWs-200/PDMS-MPI-HDI films under different healing environments; every sample for healing experiments has gone through a stretching (50%)-retracting (0%) cycle beforehand to exclude the influence of cycling numbers. As depicted in Fig. S27a, Ag NWs-200/PDMS-MPI-HDI can almost fully restore the mechanical properties in different healing environments, including high (60 °C) and low (0 °C) temperature, and artificial sweat. Except for mechanical properties, EMI shielding functions can also be recovered under these environments (Fig. S27b).

2. Supplementary Table

Table S1 Summary of the molecular weight according to GPC results

	PDMS-MPI-HDI	PDMS-MPI	PDMS-HDI
M_n	73216	68629	72968
M_w	117938	119672	126529
PDI	1.61082	1.74375	1.73403

Table S2 Summary of the healing efficiencies of PDMS-MPI-HDI for different healing time at 25 °C

Healed time	Tensile strength (MPa)	Elongation at break (%)	Healing efficiency (%)
original	0.28	1200.70	/
1 min	0.24	608.99	44.62
5 min	0.25	960.23	74.58
10 min	0.28	1180.86	97.08

Table S3. Comparison of the healing time and healing efficiency

Sample	Healing time/min	Efficiency/%	Ref.
CB[8] SP	60	33	[14]
SHP-4% GO	1	21	[15]
IP-SS	5	3	[16]
	30	10	
SPM-2	360	12	[17]
	60	17.3	
P(SPMA_{0.5}-<i>r</i>-MMA_{0.5})	180	67.9	[18]
TUEG2	60	20	[19]
Zn(Hbimcp)₂-PDMS	60	39.5	[20]
GLASSES	1440	43.9	[21]
PUU	60	62	[22]
PDMS-SS-IP-BNB	120	93	[23]
DAE-3	0.0473	90	[24]
Hydrogel	1440	98	[25]
	1	44.62	
PDMS-MPI-HDI	5	74.58	Our Work
	10	97.08	

3. Supplementary Movie

Movie S1 This movie showed the ultra-fast scratch-healing ability of PDMS-MPI-HDI at room temperature, in which the man-made scratch is able to fade away within 100s without any external interference.

References

1. J. H. Xu, S. Ye, C. D. Ding, L. H. Tan, J. J. Fu, *J. Mater. Chem. A*, 2018, **6**, 5887-5898.
2. J. H. Xu, W. Chen, C. Wang, M. Zheng, C. D. Ding, W. Jiang, L. H. Tan, J. J. Fu, *Chem. Mater.*, 2018, **30**, 6026-6039.
3. D. Döhler, J. Kang, C. B. Cooper, J. B. H. Tok, H. Rupp, W. H. Binder, Z. Bao, *ACS Appl. Polym. Mater.*, 2020, **2**, 4127-4139.
4. J. H. Xu, P. Chen, J. W. Wu, P. Hu, Y. S. Fu, W. Jiang, J. J. Fu, *Chem. Mater.*, 2019, **31**, 7951-7961.
5. Q. Qu, J. He, Y. Da, M. Zhu, Y. Liu, X. Li, X. Tian, H. Wang, *Macromolecules*, 2021, **54**, 8243-8254.
6. Z. Guo, C. Bao, X. Wang, X. Lu, H. Sun, X. Li, J. Li, J. Sun, *J. Mater. Chem. A*, 2021, **9**, 11025-11032.
7. Y. Wang, X. K. Liu, S. H. Li, T. Q. Li, S. Yu, Z. D. Li, W. K. Zhang, J. Q. Sun, *ACS Appl. Mater. Interfaces*, 2017, **9**, 29120-29129.
8. K. Huang, M. Chen, G. He, X. Hu, W. He, X. Zhou, Y. Huang, Z. Liu, *Carbon*, 2020, **157**, 466-477.
9. J. Q. Luo, S. Zhao, H. B. Zhang, Z. Deng, L. Li, Z. Z. Yu, *Compos. Sci. Technol.*, 2019, **182**, 107754.
10. W. Yuan, J. Yang, F. Yin, Y. Li, Y. Yuan, *Compos. Commun.*, 2020, **19**, 90-98.
11. C. Liu, J. Cai, P. Dang, X. Li, D. Zhang, *ACS Appl. Mater. Interfaces*, 2020, **12**, 12101-12108.
12. H. J. Sim, H. Kim, Y. Jang, G. M. Spinks, S. Gambhir, D. L. Officer, G. G. Wallace, S. J. Kim, *ACS Appl. Mater. Interfaces*, 2019, **11**, 46026-46033.
13. W. Chen, L. X. Liu, H. B. Zhang, Z. Z. Yu, *ACS Nano*, 2021, **15**, 7668-7681.
14. J. Liu, C. S. Y. Tan, Z. Yu, N. Li, C. Abell, O. A. Scherman, *Adv. Mater.*, 2017, **29**, 1605325.
15. C. Wang, N. Liu, R. Allen, J. B. H. Tok, Y. Wu, F. Zhang, Y. Chen, Z. Bao, *Adv. Mater.*, 2013, **25**, 5785-5790.
16. S. M. Kim, H. Jeon, S. H. Shin, S. A. Park, J. Jegal, S. Y. Hwang, D. X. Oh, J. Park, *Adv. Mater.*, 2018, **30**, 1705145.
17. X. Yan, Z. Liu, Q. Zhang, J. Lopez, H. Wang, H. C. Wu, S. Niu, H. Yan, S. Wang, T. Lei, J. Li, D. Qi, P. Huang, J. Huang, Y. Zhang, Y. Wang, G. Li, J. B. H. Tok, X. Chen, Z. Bao, *J. Am. Chem. Soc.*, 2018, **140**, 5280-5289.
18. J. Lee, M. W. Ming, Tan, K. Parida, G. Thangavel, S. A. Park, T. Park, P. S. Lee, *Adv. Mater.*, 2018, **30**, 1705145.
19. Y. Yanagisawa, Y. Nan, K. Okuro, T. Aida, *Science*, 2018, **359**, 72-76.
20. J. C. Lai, X. Y. Jia, D. P. Wang, Y. B. Ding, P. Zheng, C. H. Li, J. L. Zuo, Z. Bao, *Nat. Commun.*, 2019, **10**, 1164.
21. Y. Cao, Y. J. Tan, S. Li, W. W. Lee, H. Guo, Y. Cai, C. Wang, B. C. K. Tee, *Nat. Electron.*, 2019, **2**, 75-82.
22. A. Rekondo, R. Martin, A. R. D. Luzuriaga, G. Cabañero, H. J. Grande, I. Odriozola, *Mater. Horiz.*, 2014, **1**, 237-240.
23. H. Guo, Y. Han, W. Zhao, J. Yang, L. Zhang, *Nat. Commun.*, 2020, **11**, 2037.
24. Z. Xu, L. Chen, L. Lu, R. Du, W. Ma, Y. Cai, X. An, H. Wu, Q. Xu, Q. Zhang, X. Jia, *Adv. Funct. Mater.*, 2021, **31**, 2006432.
25. T. L. Sun, T. Kurokawa, S. Kuroda, A. B. Ihsan, T. Akasaki, K. Sato, M. A. Haque, T. Nakajima, J. P. Gong, *Nat. Mater.*, 2021, **12**, 932-937.